-RESEARCH PAPER-

International Journal of Mining and Geo-Engineering

IJMGE

IJMGE 57-2 (2023) 171-182

DOI: 10.22059/IJMGE.2023.352017.595006

Spectral Induced Polarization Forward Modeling in the Framework of Finite Difference Scheme

Ashkan Aliheidari [a], Seyyed Sajjad Pourhashemi [a], Reza Ghanati [a, *]

[a] *Institute of Geophysics, University of Tehran, Tehran, Iran.*

Article History:

Received: 04 December 2022.

Revised: 02 January 2023.

Accepted: 06 January 2023.

ABSTRACT

Dealing with numerous reviews and widespread inquiries, it has been concluded that much more information and interpretive parameters are accessible regarding the subsurface structures when using a particular frequency range in the spectral induced polarization (SIP) measurements. Therefore, the interpretation uncertainty would diminish which causes studies with more valid and authentic outcomes. This could be achieved by using a comprehensive and general model which is appropriate for representing electrical features variation in terms of frequency, known as the Cole-Cole model. By using the SIP method and applying a defined broad of frequencies, it would be conceivable to describe items such as medium properties, spectral behavior of the studied area, and the intensity of each single parameter. The widespread use of the SIP method requires accurate and fast modeling and inversion algorithms. An integral part of every geo-electrical data inversion is an accurate and efficient forward modeling resulting in numerical simulation of responses for a given physical property model. In other words, like every other geophysical method, a reliable spectral-induced polarization inversion is highly dependent on the accuracy of the forward problem. Forward modeling is accomplished over a 2D earth structure to generate complex resistivity data by simulating current flow into the earth's surface and solving the Poisson equation containing complex values. In this contribution, a finite difference algorithm is applied to solve the complex partial differential equations (PDEs) restricted by a mixed boundary condition. A spatial Fourier transform of the PDEs, with respect to a defined range of wavenumbers, is carried out along the strike direction to elucidate 3D source characteristics. Eventually, it is necessary to conduct an inverse Fourier transform to obtain potential solutions in the spatial domain. To verify the accuracy of the proposed numerical algorithm, some synthetic models are simulated and the forward responses, including resistance and phase values with respect to a specific frequency spectrum, are calculated. Furthermore, a comparison between our numerical results and those of Geotomo geo-electrical software is provided.

Keywords: *: Cole-Cole model, Complex resistivity, Finite difference method, Phase angle, Polarization, Spectral induced.*

1. Introduction

Electrical conduction (charge transport) and polarization (charge separation) are two principal physical properties of subsurface materials. The physical property representing either conduction or polarization phenomenon at frequencies less than 10 *kHz* is defined as complex conductivity, which can be demonstrated as a frequency-dependent complex value with both magnitude and phase. This physical parameter explicates the electrical response of a rock to an electrical excitation and illustrates its electrical behavior in terms of frequency.

The basis of geophysical data interpretation in various studies, such as exploration and environmental problems is the acquaintance of the electrical properties of rock. Electrical resistivity and polarization phenomena are applied in the geo-electrical resistivity and induced polarization methods, respectively. An alternative method called complex resistivity or equivalently, spectral induced polarization (SIP), would be generated by combining these two cited methods, in which electrical properties of rocks and minerals are measured by frequency alteration of the input signal (sinusoidal current). Due to the variation in electrical properties of rocks with frequency alteration of transmitted current, it would be feasible to reveal various physical properties of subsurface materials. With the innovation of the method, SIP has been predominantly used for mineral resources exploration, specifically sulfide deposits [1], so that the responses of measured parameters could be applicable to a more accurate recognition of these deposits and sulfide ore type determination as well [2]. Recently, owing to remarkable progress in instrumentation, forward modeling and inversion capabilities [3], the SIP method has been revisited as an auspicious tool in environmental and engineering applications. The widespread usage of the SIP method requires precise, accurate, and fast forward calculations. Furthermore, a reliable solution for sensitivity function and the inversion process is extremely dependent on the accuracy of the forward modeling.

Several probes and scrutiny have been accomplished concerning the numerical solution of the forward problem for a two-dimensional complex resistivity distribution. But early attempts in the numerical solution of electrical resistivity were focused on the potential distribution calculation without considering the effect of the frequency variation. For instance, [4] presented the basis of forward calculation based on finite-difference method. Later, an improvement in boundary conditions was presented by [5]. [6] enhanced the quality of the forward results by the singularity removal technique. But the first study on the calculation of the impedance (the ratio of complex voltage to current) distribution in terms of the frequency variation was made by [7]. [8]

* Corresponding author. Tel/Fax: +9821 61118202, *E-mail address:* rghanati@ut.ac.ir (R. Ghhanati).

developed a regularized SIP inversion method for multi-frequency IP data using the finite-element method based on the Cole-Cole model. [9] proposed a finite-element algorithm aimed at forward calculation of spectral IP responses at a set of frequencies less than 100 Hz. [10] proposed wavenumber integration using a combination of Gauss-Legendre and Gauss-Laguerre nodes. [11] presented finite-element analysis on irregularly discretized triangular meshes. [12] conducted a 2D SIP forward modeling using the finite-element method without considering electromagnetic induction. [13] represented an induced polarization forward modeling using the finite-element method and the fractal model. [14] resolved the problem for single frequencies based on complex calculus. [15] used the finite-element method to conduct 2D SIP forward modeling in 2D SIP inversion data using MPI parallel algorithm. Despite significant progresses in numerical procedures for calculating spectral induced polarization forward responses, it is still an extensively open-research area to better describe SIP signatures of soils and rocks.

In this paper, the main goal is the presentation of resistivity and phase angle pseudo-sections obtained from the forward problem solved in a 2.5-dimensional space for some synthetic arbitrarily shaped 2D structures by applying a certain electrode configuration in a specific range of frequencies.

The most widely applied numerical procedures for solving the forward modeling of SIP data can be classified into three categories, the integral equation method, the finite difference method, and the finite element method [13]. The integral equation method uses Green's function of a uniform medium and is mostly appropriate for simple and uncomplicated model geometries such as an inhomogeneous body embedded in a homogeneous medium, and it will probably fail when it comes to more flexible structures. The finite-element method is able to model an arbitrary complex 2D and 3D mediums which allows a great flexibility with respect to the geometrical shape of topography and it does not suffer from the singularity problem at the source point in a geo-electrical modeling. Some of its disadvantages can be categorized as being time-consuming and taking longer execution time compared with finite element method (FEM), requiring a forceful digital processor and the probability of notable output results varying for a certain subsurface medium. In this paper, we develop a finite difference method to numerically solve complex partial differential equations (PDEs) for arbitrarily shaped 2D bodies. One of the superiorities of this method is presenting fairly identical potential distribution for different current injection positions, so, there is no need to recalculate the potential distribution by moving the current electrode. Correspondingly, the algorithm speed would augment multiple times. Using a simple system of equations, containing sparse matrixes and small memory requirement are some of the other significant advantages of the FEM procedure.

It should be noted that all used formulations and concepts are written in the MATLAB programming language and all the pseudo-sections are derived using relevant codes and plot functions in the MATLAB medium. To ensure the fact that the implemented codes yield valid and flawless outcomes, the results will be compared to a true model mentioned in a published paper.

The Paper continues with a review of fundamental concepts of spectral-induced polarization (complex resistivity) in Section 2. Section 3 provides the basis for the forward modeling formulation. The derivation of the finite difference equation is discussed in section 4. Section 5 copes with the numerical results based on several arbitrary simulated earth models. Eventually, a brief conclusion is drawn in Section 6.

2. Methodology

Considering the fact that alternating or harmonic current is transmitted into the ground and a complex voltage is measured at the receiver, conventional analyses of SIP data comprise measuring impedance either by using multiple sinusoidal frequencies or by sampling the transient response to a pulse. The ratio of the complex electrical voltage V (or electrical potential) divided by the input electrical current I is defined as impedance, denoted by:

$$\mathrm{Z} = \frac{V}{I} \tag{1}$$

Where Z is a complex quantity containing real and imaginary components which are frequency dependent, unlike using direct current in which the ratio would be called electrical resistance which is not a complex quantity [16]. Subsequently, complex resistivity is derived by multiplying the impedance with the geometric factor K relative to the electrode array

$$\rho^* = K\mathrm{Z} \tag{2}$$

Measurements using alternating current cause a phase difference between the input current and the recorded voltage, which in this case, the complex output voltage is defined by summation of the real component (in-phase) and imaginary component (out-of-phase), thus, impedance can be represented as below:

$$\mathrm{Z}(\omega) = \mathrm{Z}_R(\omega) + \mathrm{Z}_I(\omega) \tag{3}$$

Z_R and Z_I are the measured in-phase and out-of-phase impedance components, respectively.

Theoretically, the in-phase and out-of-phase potentials alteration with frequency can bring about more information regarding the subsurface medium compared with standard DC resistivity and time-domain IP methods [17]. Hence, the SIP method could be efficient and beneficial in various terms such as extracting much more information about the studied area, distinguishing between different IP sources, and diverse subsurface properties estimation.

The frequency dependence can be expounded by models representing the general behavior of the amplitude and phase spectra in different frequency intervals and for various rock types. The most widely used one in modeling SIP effects, interpreting SIP data, discriminating different IP sources, and demonstrating electrical property variation with frequency is the Cole-Cole model, which is an empirical extension of the classic Debye relaxation model. In terms of complex resistivity, the electric voltage response to an electric current excitation can be demonstrated as [10].

$$\rho^*(\omega) = \rho_0\left(1 - m\left(1 - \frac{1}{1+(i\tau\omega)^c}\right)\right) \tag{4}$$

Where ρ_0 denotes the asymptotic resistivity value measured at zero frequency, m defines chargeability, τ time constant of the relaxation process, and c characterizes frequency dependence. In addition, ω and i stand for angular frequency and $\sqrt{-1}$, respectively. As explained above, apart from the DC resistivity ρ and chargeability m parameters used in conventional IP surveys, the Cole-Cole model holds two additional parameters, τ and c. While the parameters m and τ are related to the amount of polarizable grains and their size respectively, the exponent c is affected by the size distribution of the polarizable materials [1].

Recalling the SIP surveying process, we alluded that it is essential to record the amplitude ($|\rho|$ Ωm) and phase angle (φ rad) of the complex resistivity ρ^*over a wide frequency range, usually between 1 mHz and several kHz. Considering ρ^* as a complex number quantity, it can be mathematically formulated by amplitude and phase angle:

$$\rho^*(\omega) = \acute{\rho}(\omega) + i\,\acute{\rho}(\omega) \tag{5}$$

$$\rho^*(\omega) = |\rho|\,e^{i\varphi} = |\rho|\,(\cos\varphi + i\sin\varphi) \tag{6}$$

or equivalently in terms of conductivity

$$\sigma^*(\omega) = \acute{\sigma}(\omega) + i\,\acute{\sigma}(\omega) \tag{7}$$

$$\sigma^*(\omega) = |\sigma|\,e^{i\varphi} = |\sigma|\,(\cos\varphi + i\sin\varphi) \tag{8}$$

both the real part $\acute{\rho}$ (or $\acute{\sigma}$) and the imaginary part $\acute{\rho}$ (or $\acute{\sigma}$) are frequency dependent. Thus:

$$|\rho^*(\omega)| = \sqrt{\acute{\rho}(\omega)^2 + \acute{\rho}(\omega)^2}\ (\Omega m) \tag{9}$$

And,

$$\varphi(\omega) = arc\tan\frac{\acute{\rho}(\omega)}{\acute{\rho}(\omega)}\ (millirad)$$

since the complex resistivity ρ^* is the inverse of the complex

conductivity σ^*.

$$\rho^*(\omega) = \frac{1}{\sigma^*(\omega)} \quad (10)$$

resistivity measurements can be transformed into conductivity and vice versa. Thereupon, the equations (9) and (10) can be rewritten as follows:

$$|\sigma^*(\omega)| = \sqrt{\acute{\sigma}(\omega)^2 + \acute{\sigma}(\omega)^2}\ (S/m) \quad (11)$$

$$\varphi(\omega) = arctan\ \frac{\acute{\sigma}(\omega)}{\acute{\sigma}(\omega)}\ (millirad) \quad (12)$$

It is worth noting that the amplitude parameter correlates with the magnitude of the recorded complex resistivity and the phase angle corresponds to the phase shift between the injected current signal and the measured voltage caused by polarization [18]. Generally, the imaginary quantity is responsible for the polarization behavior of the materials.

3. Forward modelling formulation

The purpose of this section is to briefly review and analyze the mathematical formulation required to construct the forward modeling code algorithm written in the MATLAB programming language. The modeling of the electrical complex potential (the potential measured at the receiver containing real and imaginary components) is stated in terms of the partial differential equations (PDEs). To numerically solve PDEs, it is indispensable to transform them into algebraic terms. This can be implemented by using finite difference method, by which the continuous variables are represented by their values at a finite set of points and derivatives are approximated by differences between values at adjacent points. The finite difference method transforms PDEs or even ODEs, which may be nonlinear, into a system of linear equations that can be solved by matrix algebra techniques. In other words, by applying FDM, the continuous domain is discretized and the differential terms of the equation are converted into a linear algebraic equation. Modern computers can precisely implement these linear algebra computations, which along with their relative ease of implementation, has contributed to the widespread use of FDM in modern numerical analysis.

Generally, electromagnetic phenomena within material media can be macroscopically described by Maxwell's equation:

$$\nabla \times H = J \quad (13)$$

Where H *(Tesla)* denotes the magnetic field and J ($\frac{A}{m^2}$ *Ampere per meter square*) expresses the total current density:

$$J = J_c + \partial_t D + J_s \quad (14)$$

Where J_c , D ($\frac{C}{m^2}$ *Coulomb per meter square*), and J_s stand for conduction currents, dielectric displacement, and any source current, respectively. $\partial_t D$ also defines the displacement current. Assuming a linear, isotropic, and time-invariant medium in the frequency domain, the current density J and dielectric displacement D are related to the electric field E ($\frac{V}{m}$ *Volt per meter*) by electrical conductivity σ^* ($\frac{S}{m}$ *Siemens per meter*) and dielectric permittivity ε^* ($\frac{F}{m}$ *Farad per meter*), respectively.

$$J = \sigma^*(\omega) E \quad (15)$$

$$D = \varepsilon^*(\omega) E \quad (16)$$

The last two equations describe the electrical properties of the subsurface medium as a scalar function of angular frequency ω. Since the electric field is stationery and curl-free (in the absence of magnetic sources $\partial_t B = 0$), which means $\nabla \times E = 0$, it can be written as:

$$E = -\nabla\phi^* \quad (17)$$

Which ϕ^* indicates a complex scalar potential, and $*$ denotes a complex value. By recalling equation (16) and combining it with equation (18), it yields:

$$J = -\sigma^*(\omega)\nabla\phi^* \quad (19)$$

Applying the charge conservation theory over a volume and continuity equation to the recent equation, it is obtained:

$$\nabla \cdot J = \frac{\partial p}{\partial t}\ \delta(x - x_s)\delta(y - y_s)\delta(z - z_s) = -I\ \delta(r - r_s) \quad (20)$$

Where p ($\frac{C}{m}$ *Coulomb per meter*) denotes the charge density specified at a point in the Cartesian $x - y - z$ space, δ delta Dirac function, and $r_s = (x_s, y_s, z_s)$ indicates the coordinates where the current is fed into the ground in the $x - y - z$ space. Since any arbitrary electrode configuration can be applied via pertinent superposition, here only a single electrode current source needs to be considered. This shall be indicated as a point source at r_s.

Regarding equations (16) and (19), it has been displayed that the conductivity is a complex and frequency-dependent quantity. In other words, the electric field E and the conduction current density J are not necessarily in-phase, but rather might hold both in-phase and out-of-phase values. Considering Maxwell's equation again, it can be rewritten using frequency-dependent complex quantities which are σ and ε :

$$\nabla \times H = (\sigma^*(\omega) + i\,\omega\varepsilon(\omega))E + J_s + \partial_t D \quad (21)$$

Equation (21) represents Maxwell's equation in the frequency domain. Regarding Equation (21), the quasi-static theory $\frac{\omega|\varepsilon|}{|\sigma|} \ll 1$ can be considered and applied for normal earth material on the condition that the $f = \frac{\omega}{2\pi} < 10\ kHz$ criterion is met. Therefore, the conventional displacement currents $\partial_t D$ can be neglected. So, the previous equation turns into:

$$\nabla \times H = \left(\sigma^*(\omega) + i\omega\varepsilon(\omega)\right) E + J_s \quad (22)$$

By taking the divergence of equation (22), it eventually yields:

$$\nabla \cdot (\sigma^*(\omega)E) - \nabla \cdot J_s = 0 \quad (23)$$

Which will grow into the well-known Poisson equation considered as the basis of the forward modeling algorithm. It is reminded that equation (23) is mathematically utterly identical to the conventional DC resistivity problem one, except that it is stated at an appointed frequency ω.

Having obtained all these relations, if we merge the equations (23) and (18), it leads to the following equation:

$$-\nabla \cdot (\sigma^*(\omega)\nabla\phi^*(\omega)) - \nabla \cdot J_s = 0 \quad (24)$$

Hence, it can be written for a three dimensional medium as:

$$-\nabla \cdot (\sigma^*(x,y,z)\nabla\phi^*(x,y,z)) = \frac{\partial p}{\partial t}\ \delta(x - x_s)\delta(y - y_s)\delta(z - z_s) \quad (25)$$

With the assumption that the y direction is considered parallel as strike direction of the model and there would be no charge in the conductivity distribution of strike direction, we obtain:

$$\frac{\partial}{\partial y}(\sigma^*(x,y,z)) = \quad (26)$$

Henceforth the complex conductivity can be presented as :

$$\sigma^*(x,y,z) = \sigma^*(x,z) \quad (27)$$

accordingly, equation (25) is rewritten as:

$$-\nabla \cdot (\sigma^*(\omega,x,z)\nabla\phi^*(\omega,x,y,z)) = \frac{\partial p}{\partial t}\ \delta(x - x_s)\delta(y - y_s)\delta(z - z_s) \quad (28)$$

Similarly, it can be presented like this :

$$\nabla \cdot (\sigma^*(\omega,x,z)\nabla\phi^*(\omega,x,y,z)) = -I\ \delta(x - x_s)\delta(y - y_s)\delta(z - z_s) \quad (29)$$

By applying some elementary vector calculus on equation (28) and considering the fact that:

$$\nabla\sigma^* \cdot \nabla\phi^* = \frac{I}{2}\left(-\sigma^*\nabla^2\phi^* + \nabla^2(\sigma^*\phi^*) - \phi^*\nabla^2\sigma^*\right) \quad (30)$$

By substituting the former relation for equation (29), we obtain:

$$\sigma^*(\omega,x,z)\nabla^2\phi^*(\omega,x,y,z) - \phi^*(\omega,x,y,z)\nabla^2\sigma^*(\omega,x,z) + \nabla^2\left(\sigma^*(\omega,x,z)\phi^*(\omega,x,y,z)\right) = -I\,\delta(x-x_s)\delta(y-y_s)\delta(z-z_s) \quad (31)$$

Equation (31), which is another form of the Poisson equation illustrated in equation (23) and generated by acting upon some mathematical operations, is considered as the main governing equation, equivalently a PDE, defining the forward problem in the frequency domain.

Before proceeding further with the discussion, it is preferable to remark on two important tips assumed in all forward modeling processes. Considering the first case, it is stated that within the scope of this paper, only the electrical properties of rocks at frequencies less than 10 kHz are of interest. At this scale, polarization effects entailing the movement of charge carriers over distances up to the order of centimeters give rise to the observed delay of the response to an impressed excitation. Propounding the second case, we assume that the region of interest may be served as a 2D complex resistivity distribution. However, the source used in geo-electrical prospection is assumed to hold a 3D distribution (the electrical potential distribution $\phi^*(\omega,x,y,z)$ due to a point source is 3D). Consequently, the problem can be considered as a 2.5D one [19]. To put it in another way, the advantage of a 2.5D approach is that a physically realistic representation, involving a 3D source, is obtained by solving several problems with a 2D geometry in the wavenumber domain. Hence, the computational time is exceptionally decreased compared to a full 3D modeling process. Therefore, the first and essential step would be formulating and solving a 2.5D complex resistivity forward modeling. To do so, the Poisson equation discussed heretofore is used to simulate the current flow into the earth.

In order to reckon on 3D source characteristics and for computational simplicity, we need to perform a spatial Fourier transform on the partial differential equations by transforming y into the k_y domain with regard to a range of wavenumbers along the strike direction, in order to solve the equations in Fourier transformed space (x,k_y,z) . This transformation is functioned in the forward and backward direction by the following two equations. Since $\phi\,(x,y,z)$ is even in y direction, it is obtained as:

$$\tilde{\phi}(x,k_y,z) = 2\int_0^{\infty}\phi(x,y,z)\cos(ky)\,dy \quad (32)$$

$$\phi^*(x,y,z) = 2/\pi\int_0^{\infty}\tilde{\phi}(x,k_y,z)\cos(k_y y)\,dk_y \quad (33)$$

Where $\tilde{\phi}$ and k denote the transformed complex potential in the Fourier domain and real wavenumber, respectively.

By applying the mathematical definition of equation (32) to the potential quantity in Poisson equation (31), the three-dimensional potential distribution $\phi(x,y,z)$ due to a point source at (x_s,y_s,z_s) over a 2D complex conductivity distribution $\sigma^*(\omega,x,z)$ is reduced to a 2D transformed potential $\tilde{\phi}(x,k_y,z)$, which is a solution of the equation (31).

$$\sigma^*(\omega,x,z)\,\nabla^2\tilde{\phi}(x,k_y,z) - \tilde{\phi}(x,k_y,z)\nabla^2\sigma^*(\omega,x,z) + \nabla^2\left(\sigma^*(\omega,x,z)\,\tilde{\phi}(x,k_y,z)\right) - 2k_y^2\,\sigma^*(\omega,x,z)\,\tilde{\phi}(x,k_y,z) = -I\,\delta(x-x_s)\,\delta(y-y_s)\,\delta(z-z_s) \quad (34)$$

And similarly:

$$-\nabla\cdot(\sigma^*(\omega,x,z)\nabla\tilde{\phi}(x,k_y,z)) + k_y^2\,\sigma^*(\omega,x,z)\,\tilde{\phi}(x,k_y,z) = -I\,\delta(x-x_s)\delta(y-y_s)\delta(z-z_s) \quad (35)$$

Which is a 2D partial differential equation known as the Helmholtz equation, which has to be solved for a 2D domain restricted by mixed boundary conditions regarding several discrete wavenumbers. The boundary conditions are

1) $\phi^*(\omega,x,y,z)$ must be continuous across each boundary of the physical property distribution of $\sigma^*(\omega,x,z)$.
2) The normal component of J must be continuous across each boundary as well.

The main objective is to calculate $\tilde{\phi}(x,k_y,z)$. A proper discretization of the $(x,\,k_y,\,z)$ space in the form of a rectangular grid with nodes at the cell center is required to numerically solve the equation (34). In this contribution, a finite difference algorithm is applied to discretize the simulated models restricted by mixed boundary conditions. (One of the privileges of the finite difference method over other ones is its capability to quickly approximate the solution for any arbitrary and complex structure models and also its higher speed against the finite element method).

The generalized form of equations (34) and (35) can be demonstrated as:

$$-\frac{\partial}{\partial x}\left(P(x,z)\,\frac{\partial\tilde{\phi}}{\partial x}(x,k_y,z)\right) - \frac{\partial}{\partial z}\left(P(x,z)\,\frac{\partial\tilde{\phi}}{\partial z}(x,k_y,z)\right) + \sigma^*(x,z)\,\tilde{\phi}(x,k_y,z)) = f(x,z) \quad (36)$$

This statement is defined in a set of $\Re$, which is assumed to be closed and connected to have a sufficiently regular boundary. The P and f functions are at least piecewise continuous in $\Re$.

To define a semi-infinite half-space medium with an arbitrary complex conductivity distribution, the set of $\Re$ is arranged for artificial boundaries simulating infinitely distant planes in both the horizontal (x-direction) and vertical (z-direction) extent. Such a half-space is indicated by the grid shown in figure 1.

The grid is chosen to be rectangular with an arbitrary irregular spacing of the nodes in the the x and z directions. The rectangular grid comprising nodes in the x direction and z direction are indicated by $i = 1,2,3,\ldots,N$ and $j = 1,2,3,\ldots,M$, respectively. Considering the left, right and bottom infinite edges of the half-space, they are designed by the lines $i = 1$, $i = N$ and $j = M$, respectively.

Therefore, choosing a sufficiently large number of M and N and applying mentioned boundary conditions, will lead to the infinite edges simulation by a finite choice of M and N. The representative equation (34) is then applied to any existing node (i,j) in the grid to yield an approximate complex potential quantity over area ΔA, which is illustrated by the hatched portion in figure 1.

$$\Delta A = \frac{(\Delta x_i+\Delta x_{i-1})\times(\Delta z_j+\Delta z_{j-1})}{4} \quad (37)$$

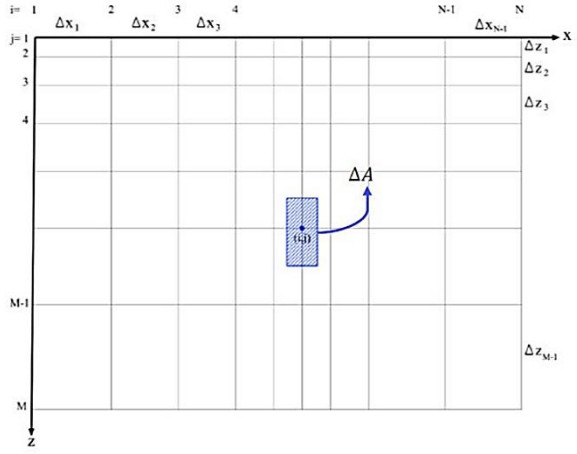

Figure 1. Rectangular discretization grid used to discretize the transformed equation (34). Discretization is usually implemented in both directions so that the intervals are considered major near the boundaries and become more minor as approaching to center of the studied area. Subsequently, the middle medium recedes from the boundary conditions.

After constructing a discrete model in the form of rectangular grids, the next step is replacing the existing partial derivatives with finite difference formula.

4. Derivation of the finite difference equation

Discretization in the framework of the finite difference method can be applied in two ways, discretization by points and discretization by area. The first approach deals with the known physical property

distribution, the complex conductivity $\sigma^*(\omega,x,z)$, which has to be discretized at each node by $\sigma^*_{i,j}$. Then, in terms of the numerical solution, a discrete set of $\tilde{\sigma}_{i,j}$ at each node has to be evaluated. In this paper, the first approach is ignored and it is concentrated on the second one, discretization by area.

As mentioned in the third section, at any node in the set of $\Re$, the fundamental relation for the desired unknown potential $\tilde{\phi}(x,k_y,z)$can be presented by the following partial differential equation:

$$-\nabla\cdot(\sigma^*(\omega,x,z)\nabla\tilde{\phi}(x,k_y,z)) + k_y^2\,\sigma^*(\omega,x,z)\,\tilde{\phi}(x,k_y,z) = -I\,\delta(x-x_s)\delta(y-y_s)\delta(z-z_s) \quad (38)$$

Here, the physical property distribution $\sigma^*(\omega,x,z)$ at any node (i,j) of the rectangular grid indicates the conductivity in a region restricted by the nodes (i,j) and $(i+1,j)$ in the x-direction and the nodes $(i,j+1)$ and $(i+1,j+1)$ in the z-direction. The aim is to evaluate the numerical solution of equation (34) that contains a discrete set of $\tilde{\sigma}_{i,j}$ at each node. The four side-bounded regions are illustrated in figure 2, holding the previously mentioned equation (37)

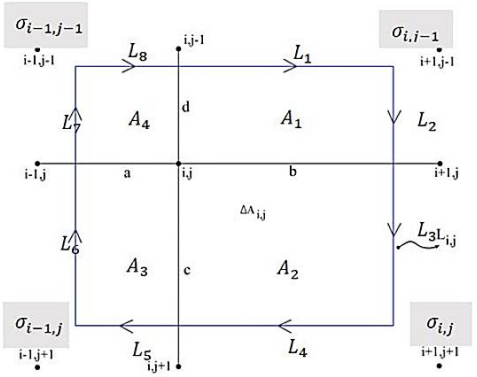

Figure 2. Illustration of the discretized area element ΔA_{ij} ,followed by a detailed description of $\tilde{\sigma}_{i,j}$ distribution at the representative mesh area ΔA_{ij} and the line contour L_{ij} about the node (i,j)

As indicated above, the contour integration along the line L_{ij} is subdivided into 8 subsections.

For each node (i,j), for which $\tilde{\sigma}_{ij}$ is unknown, the equation (37) is integrated over the corresponding mesh region ΔA_{ij} to obtain:

$$-\iint_{\Delta A_{ij}}\nabla\cdot\left(\sigma^*(x_i,z_j)\nabla\tilde{\phi}(x_i,k_y,z_j)\right)dx_i dz_j + \iint_{\Delta A_{ij}}k_y^2\left(\sigma^*(x_i,z_j)\tilde{\phi}(x_i,k_y\,z_j)\right)dx_i dz_j = \iint_{\Delta A_{ij}}\frac{I}{2}\delta(x-x_s)\delta(y-y_s)\delta(z-z_s)dx_i dz_j \quad (39)$$

The next step is applying Green's theorem integrating along the entire path L_{ij}. It is noted that to refrain from using complicated mathematical formulations in this step, some processes of obtaining the main required formulation are dropped. The detailed explanation can be found in [4].

Eventually, the self-joint difference equation indicates the solution of $\tilde{\phi}$ at node (i,j) which is dependent only on the values of $\tilde{\phi}$ at the adjacent nodes $(i-1,j),(i+1,j),(i,j-1)$ and $(i,j+1)$ are related to each other by:

$$C_L^{ij}\tilde{\phi}_{i-1,j} + C_R^{ij}\tilde{\phi}_{i+1,j} + C_T^{ij}\tilde{\phi}_{i,j-1} + C_B^{ij}\tilde{\phi}_{i,j+1} + C_P^{ij}\tilde{\phi}_{i,j} = \frac{I}{2}\,\delta(x-x_s)\,\delta(z-z_s) \quad (40)$$

Where,

$$C_L^{ij} = -\frac{\Delta z_{j-1}\sigma^*_{i-1,j-1}+\Delta z_j\sigma^*_{i-1,j}}{2\Delta x_{i-1}} \quad (41)$$

C_L^{ij} is the self-coupling coefficient in the left x-direction between nodes (i,j) and $(i-1,j)$

$$C_R^{ij} = -\frac{\Delta z_{j-1}\sigma^*_{i,j-1}+\Delta z_j\sigma^*_{i,j}}{2\Delta x_i} \quad (42)$$

C_R^{ij} is the self-coupling coefficient in the right x-direction between nodes (i,j) and $(i+1,j)$.

$$C_T^{ij} = -\frac{\Delta x_{i-1}\sigma^*_{i-1,j-1}+\Delta x_i\sigma^*_{i,j-1}}{2\Delta z_{j-1}} \quad (43)$$

C_T^{ij} is the self-coupling coefficient in the top z-direction between nodes (i,j) and $(i,j-1)$.

$$C_B^{ij} = -\frac{\Delta x_{i-1}\sigma^*_{i-1,j}+\Delta x_i\sigma^*_{i,j}}{2\Delta z_j} \quad (44)$$

C_B^{ij} is the self-coupling coefficient in the bottom z-direction between nodes (i,j) and $(i,j+1)$.

$$C_P^{ij} = -\left(C_L^{ij} + C_R^{ij} + C_T^{ij} + C_B^{ij} - A(\sigma^*_{ij},A_{ij})\right) \quad (45)$$

C_P^{ij} is the self-coupling coefficient at position (i,j), in which $A(\sigma^*_{ij},A_{ij})$ is defined as:

$$A(\sigma^*_{ij},A_{ij}) = \frac{1}{4}\,k_y^2(\sigma^*_{i,j-1}\Delta x_i\Delta z_{j-1} + \sigma^*_{i,j}\Delta x_i\Delta z_j + \sigma^*_{i-1,j}\Delta x_{i-1}\Delta z_j + \sigma^*_{i-1,j-1}\Delta x_{i-1}\Delta z_{j-1}) \quad (46)$$

The self-coupling functions are known functions related to geometry and physical property distribution and have nothing to do with the position of the current electrode.

Equation (40) is a linear equation containing five potentials: one main potential at the center and four adjacent potentials surrounding it. This equation is valid for a single node, particularly (i,j). The process should be carried out by calculating the equation for all nodes. Once the process is implemented and the discrete representation for the governing equations and boundary conditions at all existing nodes is achieved, the transformed forward problem can be written as a set of simultaneous equations for all the nodes in the grid:

$$C^*\,\tilde{\phi} = q \quad (47)$$

In which q denotes the source vector and C represents $MN\times MN$ complex, sparse, symmetric five-band capacitance matrix containing all self-coupling coefficients, and it is a function of geometry and physical property distribution in the grid. It is worth mentioning that for multiple source locations, matrix C remains unaltered. Hence, only one inversion of C in terms of different wavenumbers provides the solution with different sets of vectors $\tilde{\phi}$ for the various source positions.

Formerly, it was mentioned that the equation (47) has to be solved for vector $\tilde{\phi}$, which contains potentials for all existing nodes.

$$\tilde{\phi} = (C^*)^{-1}\,q \quad (48)$$

For this purpose, it is required to reverse the formerly-calculated capacitance matrix and multiply it by the source vector. Once the operation is accomplished computing the Fourier transformed potential for a sufficiently large number of discrete wavenumbers k, an inverse Fourier transform is implemented then to obtain the potential solutions in the spatial domain $\phi^*(r)$.

$$\phi^*(x,y,z) = \frac{2}{\pi\int_0^\infty\tilde{\phi}(x,k_y,z)\cos(k_y y)dk_y} \quad (49)$$

Which $\phi^*(x,y,z)$ indicates 3D complex potential distribution.

Note that further details about the solution of the governing equations as well as the discretization of the model in terms of the finite difference algorithm can be found in [4].

As mentioned beforehand, a complex quantity holds in-phase and out-of-phase components (real and imaginary parts or equivalently, amplitude and phase). Once the in-phase and out-of-phase values are available, the amplitude and phase angle can be obtained using:

$$|\sigma^*(\omega)| = \sqrt{\sigma'(\omega)^2+\sigma''(\omega)^2} \quad (50)$$

$$\varphi(\omega) = arc\,tan\,\frac{\sigma''(\omega)}{\sigma'(\omega)} \quad (51)$$

It is noted that the two previous equations can be illustrated in the form of complex resistivity as well.

5. Synthetic test models

In this section, the results from three synthetic tests of forward

modeling using the finite difference method are presented. Synthetic case studies are used to verify and evaluate the accuracy and efficiency of the numerical strategy for 2.5D forward modeling from both geometrically simple and complicated body. In the first two synthetic models, two relatively complex models are used, while, the third model has been derived from a published article in which the pseudo-sections are presented and the results are compared with those in the published paper. It is noteworthy that the presented results consist of amplitude and phase angle pseudo-sections. All the computations were carried out on a 1.9 GHz Core (TM) i5-based desktop PC.

Before further proceeding, as all the discussed methods deal with complex resistivity, it is first needed to generate complex apparent resistivity (or conductivity) data using the MATLAB code in order to construct various geological models and compare their responses with observed data to obtain a valid model for the area of interest. All the relations mentioned in the following are basically dependent on complex resistivity values. The substantial necessity in all mentioned cases is gaining acquaintance of complex resistivity values in a discretized half-space medium for an arbitrarily shaped structure. In other words, it is required to appoint a specific complex resistivity value to every single discretized cell. To do so, first, considering a slightly arbitrary geological structure, the rectangular-shaped cell medium should be parameterized with constant resistivity, chargeability, time constant, and frequency-dependent constant in every single existing cell. Once the four parameters are attributed to each cell, according to the geological structure, henceforth, it is required to apply the Cole-Cole model to obtain complex resistivity, attributed to each cell:

$$\rho^*(\omega) = \rho_0 \left(1 - m \left(1 - \frac{1}{1+(i\tau\omega)^c}\right)\right) \quad (52)$$

or equivalently,

$$\sigma^*(\omega) = \sigma_0 \left(1 + \frac{m}{1-m} \left(1 - \frac{1}{1+(i\tau\omega)^c}\right)\right) \quad (53)$$

Now, a 2D complex resistivity $\rho^*(\omega)$ distribution is available to be used in the next steps.

5.1. Model 1

The first synthetic model consists of five different mediums in terms of Cole-Cole parameters. There are two consecutive layered mediums, starting from the ground surface, with 4 m and 3 m thicknesses, respectively. Two structures are embedded in a relatively conductive medium. An inclined dyke with 100 m width is stretches from the bottom of the second layered medium toward the bedrock. Also, there is a 10 m × 50 m polarizable box located at the southeast of the main medium (Figure 3). Table 1 also represents the geological structures simulated in the first synthetic model.

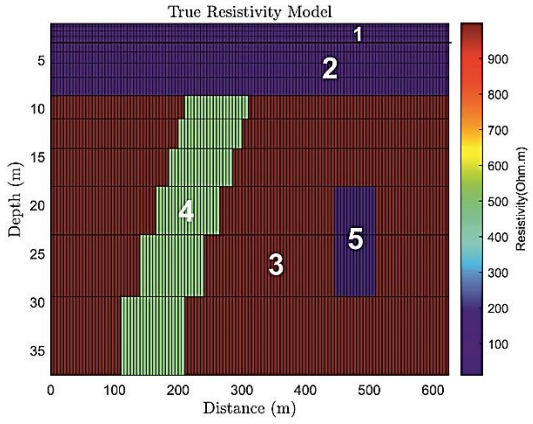

Figure 3. Representation of the first synthetic model containing five different mediums.

The in-phase and out-of-phase apparent impedance values for the 2D synthetic model shown in Fig.3 are calculated for ten frequencies using the finite difference method. The frequency values are 0.001, 0.01, 0.1, 1, 10, 100, 500, 1000, 5000, and 10000 Hz. It is essential to remark that this wide frequency range is necessary in order to obtain reliable values for characteristic parameters. However, in real field measurements, the highest and lowest used frequencies are limited by practical limitations. The lowest frequency value is limited by the available survey time, for example, a frequency of 0.001Hz requires 1000 s per cycle, while each measurement technically needs at least several cycles. The highest frequency is limited by EM coupling, which sets mostly a limit between 10 to 100 Hz.

Table 1. Five different environmental regions used in the first synthetic model.

Number	Region
1	First layered medium 4 meters' thickness
2	Second layered medium 3 meters' thickness
3	Relatively conductive medium
4	Inclined dyke
5	Polarizable box

The in-phase and out-of-phase apparent impedance values for the 2D synthetic model shown in Fig.3 are calculated for ten frequencies using the finite difference method. The frequency values are 0.001, 0.01, 0.1, 1, 10, 100, 500, 1000, 5000, and 10000 Hz. It is essential to remark that this wide frequency range is necessary in order to obtain reliable values for characteristic parameters. However, in real field measurements, the highest and lowest used frequencies are limited by practical limitations. The lowest frequency value is limited by the available survey time, for example, a frequency of 0.001Hz requires 1000 s per cycle, while each measurement technically needs at least several cycles. The highest frequency is limited by EM coupling, which sets mostly a limit between 10 to 100 Hz.

The apparent impedance values are calculated by applying the Dipole-Dipole array for 9 n-level. While the amount of the injected current is 1A, the number of stations is 40, and the electrode spacing is considered as 15 m. As mentioned beforehand, it is required to determine 4 Cole-Cole parameters for each desired medium. The quantities of the Cole-Cole parameters for the first synthetic model are presented in Table 2.

Table 2. Properties of the first synthetic model region illustrated in Figure .3 based on the Cole-Cole model parameters: Resistivity ρ, chargeability m, time constant τ, and frequency dependence c which is a dimensionless quantity

Number	Region	ρ (Ωm)	m (mV/V)	τ(s)	c (-)
1	Layered earth 1	150	0.035	0.6	0.45
2	Layered earth 2	75	0.4	0.1	0.5
3	Background	1000	0.01	0.3	0.6
4	Inclined dyke	500	0.1	0.5	0.75
5	Box	10	1	0.05	0.2

Applying the finite difference algorithm written in the MATLAB programming language to the determined synthetic model, the outcome of amplitude and phase angle pseudo-sections in terms of the different frequency ranges are illustrated in Figure 4 and Figure 5, respectively.

As shown in Fig.4, no substantial variations are detected in ten pseudo-sections and all of them can be considered identical. Although, a roughly 2-layer behavior is observed and well resolved. Moreover, existing values in pseudo-sections acceptably conform to the chosen quantities in the synthetic model. Due to the nearby contrast of the inclined dyke with its inclusive surroundings, it has not been resolved well, but there is a region, particularly with a lower resistivity quantity in approximate distance of 200 to 250 m from the beginning of the profile, which represents the lower-resistive inclined dyke rather than the higher-resistive surrounding. Along the higher-resistive setting, beginning from the approximate depth of 22 m and extending to the end of the pseudo-section while encompassing the whole lower part of it, at an approximate distance of 480 m from the outset of the profile, a region with a much lower resistivity quantity than the surrounding

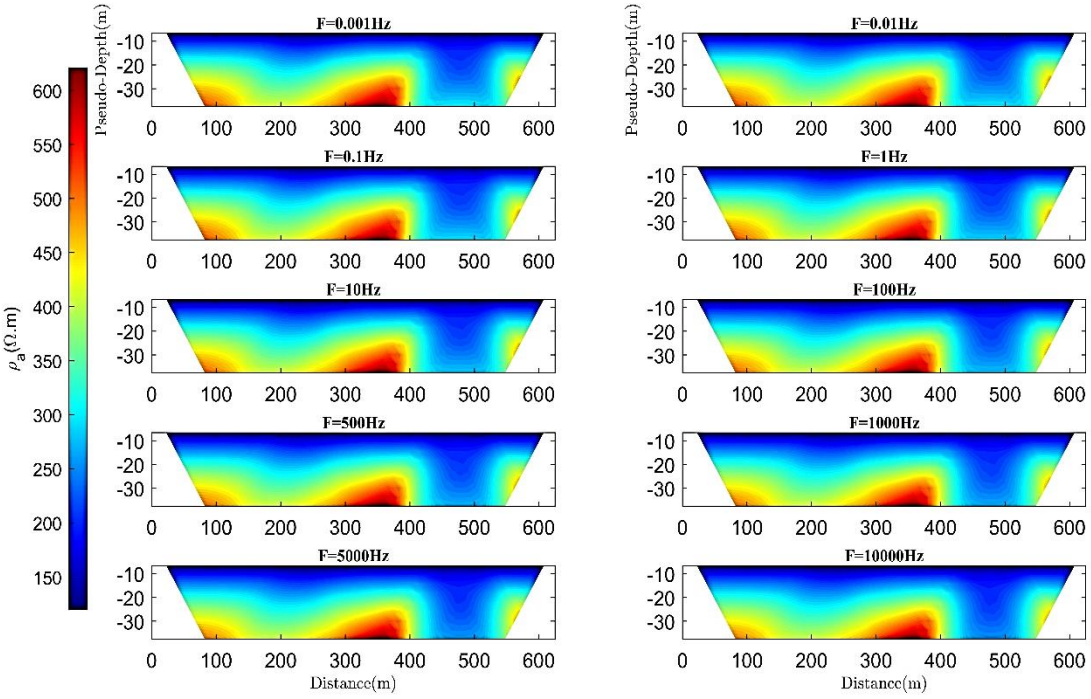

Figure 4. Apparent resistivity (amplitude) pseudo-sections for the first synthetic model shown in Fig.3, in terms of ten different frequency values.

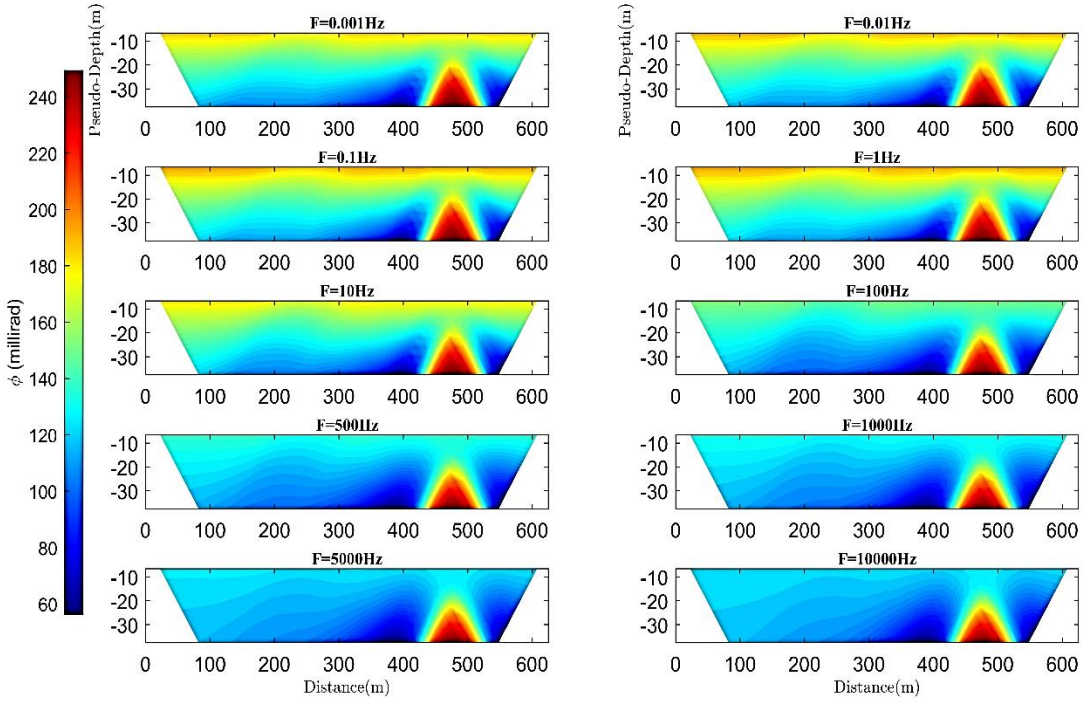

Figure 5. Phase angle pseudo-sections for the first synthetic model shown in Fig.3, in terms of ten different frequency values.

setting is observed that can be interpreted as the conductive block named by number 5 in the synthetic model, which resistivity is prominently lower than medium 3. It should be noted that some artifacts towards the bottom boundary and below the second layered medium can be observed, which is probably due to the effect of the boundary conditions.

Heeding the phase angle pseudo-sections, it is obvious that the inclined conductive dyke cannot be distinguished by applying higher frequencies, probably due to its lower contrast with the surrounding setting. As the frequency decreases, the inclined dyke is marked more clearly. It is probably deduced that two low-contrast mediums can be distinguished using a broad range of frequencies rather than one single frequency. Despite amplitude pseudo-sections, another noteworthy tip about phase pseudo-sections is their clear discrepancy from each other

over applying a broad range of frequencies, so that the form of anomalies in every single pseudo-section differs remarkably from others.

5.2. Model 2

The second model is composed of three different geological phenomena. A joined continuous tectonic uplift and graben with an approximate length of 40 m attaches the first and second medium to each other. These two mediums share a smooth boundary in the following. The second medium is more conductive than the first one and holds much more chargeability value as well. There is also a more conductive 2 $m \times 10$ m box than the two previous mediums embedded in the east part of the second medium with the relative distance of 60 m from the outset of the profile (see Fig. 6). Table 3 also lists these tectonic phenomena.

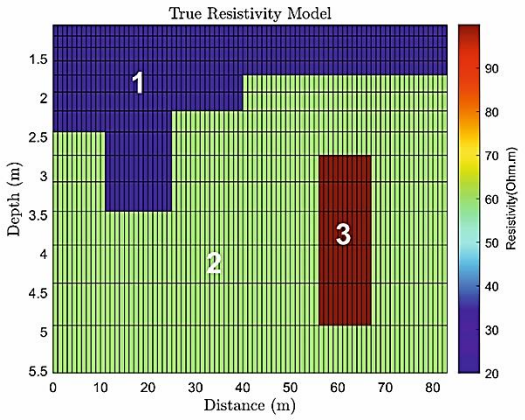

Figure 6. Representation of the second synthetic model containing three different mediums.

The in-phase and out-of-phase apparent impedance values for a 2D model shown in Fig.6 are calculated for ten frequencies, different from the ones used in the previous model (i.e., 0.001, 0.01, 0.1, 1, 10, 20, 50, 100, 500, 1000 Hz). The same Dipole-Dipole electrode array is used for the simulations of the second model, so that the apparent impedance values are calculated for the 10 n-level. While the amount of the injected current is 1A, the number of stations is chosen to be 40 and the electrode spacing is considered as 2 m. The values of the Cole-Cole parameters for the second synthetic model are summarized in Table 4.

Table 3. Three different environmental regions simulated in the second synthetic model.

Number	region
1	Medium 1
2	Medium 2
3	Box

Table 4. Properties of the second synthetic model region illustrated in Fig.6 based on the Cole-Cole model parameters: Resistivity ρ, chargeability m, time constant τ and frequency dependence c which is a dimensionless quantity.

Number	Region	ρ (Ωm)	m (mV/V)	τ(s)	c (-)
1	Medium1	20	8	0.006	0.4
2	Medium2	60	90	0.0015	0.7
3	Box	100	45	0.09	0.55

Considering the Cole-Cole model parameters for each medium, the potential response of the simulated earth model is calculated using the proposed finite difference algorithm at different frequencies. Figure 7 and Figure 8 show the retrieved apparent amplitude and phase distributions for all frequencies, respectively.

As seen in Figure 7, the first point that comes to mind is just like the first model, the amplitude images are not altering much along frequency variation and look analogous. Nevertheless, the sites and quantities of phenomena have been retrieved perfectly. The first medium, which is observed clearly in the southwest region of the pseudo-section (left-hand side), is considered a more resistive than the second medium, representing a low-resistance region depicted by blue color. As we proceed towards the east part of the pseudo-section, the effect of the first medium is diminished. This might be because of the presence of the third medium, which is much more conductive than the first two models.

According to the phase angle pseudo-sections shown in Fig.8, in contrast to the amplitude pseudo-sections which do not vary along different frequencies, the phase angle images are more interesting and show quite different anomalies than amplitude. Although it does not show remarkable changes and looks like a smooth spectral behavior at first glance, by more accurate analysis and more detailed review, some discrepancies over a broad range of frequencies are observable. It should be mentioned that the phase pseudo-sections sharply delineate the whole conductive block and two other mediums. Despite not representing clear alteration for the first two mediums on the left-hand side of the pseudo-sections, by considering the polarizable box on the right-hand side at low frequencies, the phase images show values up to 0.06 $mrad$ and as we proceed to higher frequencies, the phase decreases up to 0.02 $mrad$ and fades out in terms of the intensity of anomaly.

5.3. Model 3

In order to assure reliability and evaluate the efficiency of the written the MATLAB code algorithm, the pseudo-sections obtained from the written code were tested by the outcome of a synthetic model used by [9]. The goal is to provide a visual comparison between our numerical results and those obtained by [9] in terms of amplitude and phase pseudo-sections.

The last synthetic model consists of two rectangular blocks embedded in a uniform medium of resistivity of 10 Ωm, chargeability of 10 mV/V, a time constant of 1 s and a relaxation constant of 0.2 (Fig.9). The Cole-Cole parameters of these two blocks are set to be different from the background medium, instead of a totally homogenous model. Table 5 represents the Cole-Cole parameters associated with example 3. Both rectangular blocks have a transitional layer to simulate the smooth variation in the electrical parameters.

Considering Fig.9, the apparent impedance values for this 2D model are calculated at ten frequencies (i.e., 0.001, 0.01, 0.1, 1, 10, 20, 25, 50, 100, and 1000 Hz) using the finite difference method.

The complex apparent electrical resistivity responses of the synthetic model are simulated using the linear dipole-dipole configuration from position 0 up to 25 m with fixed electrode spacings of 1 m up to 10 levels ($n = 1 - 10$, where n indicates the number of receiver-transmitter dipole separation). Figures 10 and 11 indicate the resistivity and phase pseudo-sections derived from the third synthetic model, respectively.

In addition, for further appraisal, the resulting simulations of the corresponding synthetic example are compared with those represented by [9] for the frequency of 1 Hz (see Fig. 12 and 13). In spite of calculating the apparent complex impedance values for the defined frequency range, it is noted that the comparison is only done for the frequency of 1 Hz (the same frequency used by [9]).

Visually comparing the resulting pseudo-sections, it is observed that there is a trivial difference between the apparent resistivity and phase contours obtained from the proposed algorithm and those from [9]. The left block is less well resolved, probably due to its lower contrast with the surrounding medium compared to the right block. As mentioned earlier, The right block is perfectly resolved due to its sufficient contrast with the surrounding medium. Although, as we proceed to higher frequencies, the left block is much better presented at the lower frequencies. It is probably concluded that even a minor contradiction of

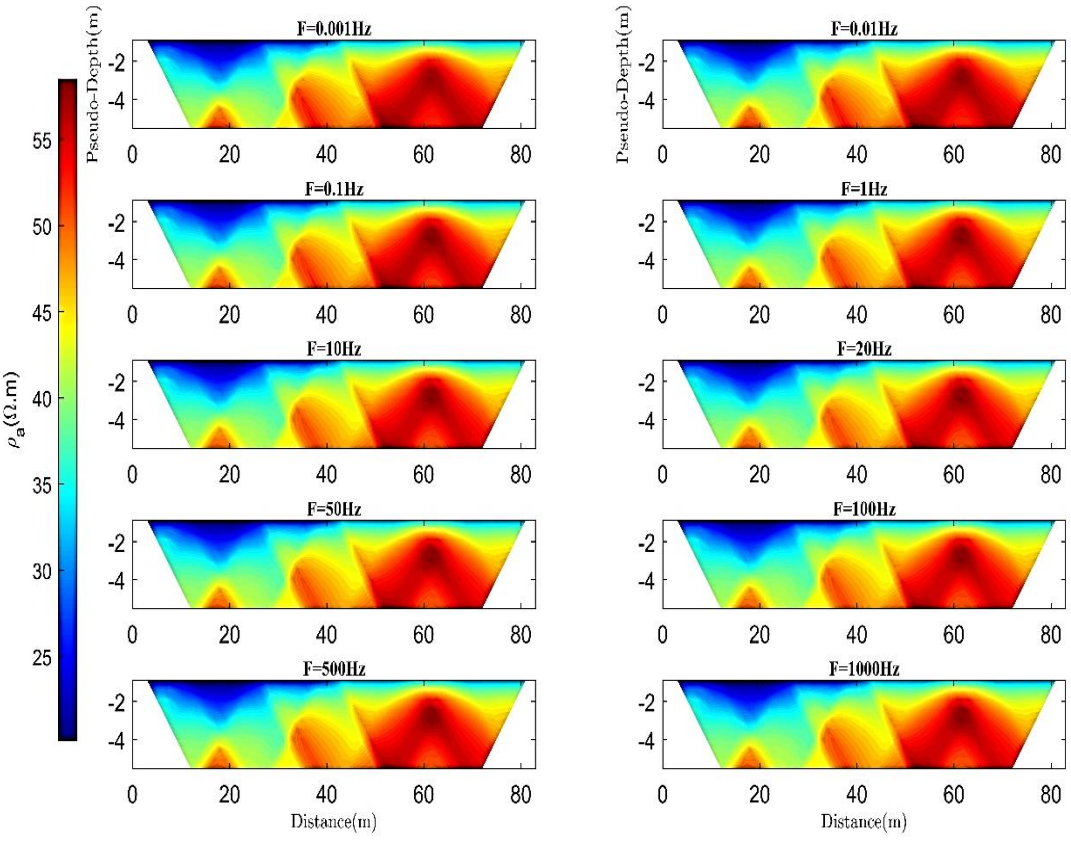

Figure 7. Apparent resistivity (amplitude) pseudo-sections for the second synthetic model shown in Fig.6, in terms of ten different frequency values.

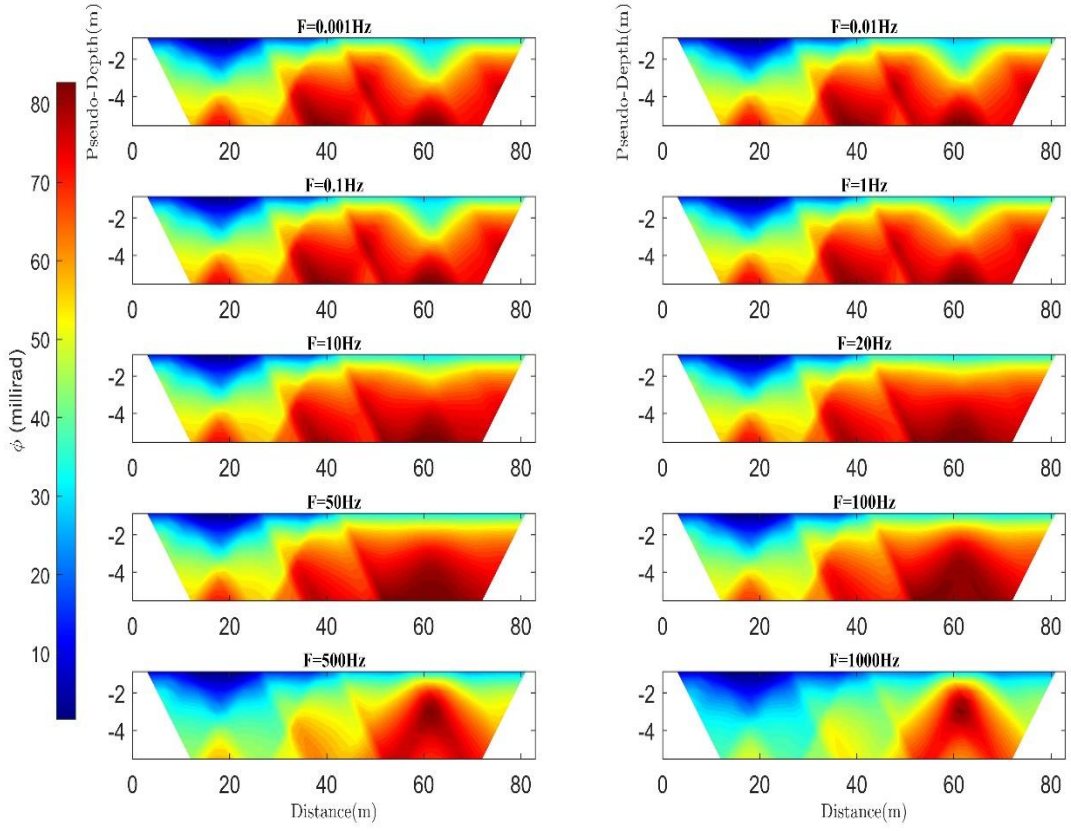

Figure 8. Phase angle pseudo-sections for the second synthetic model shown in Fig.6, in terms of ten different frequency values.

a specific medium with its surrounding setting would be distinguished by applying a broad range of frequencies, while only a single frequency usage in this matter would presumably fail. Just like conclusions obtained from the last two synthetic models, no remarkable variation in amplitude pseudo-sections can be observed, and it seems that the use of SIP might be somewhat useless. But the variations are obvious and discernible if Cole-Cole parameters sections are obtained by applying the inversion algorithm thereinafter.

Table 5. Properties of the third synthetic model region illustrated in Figure 9 based on the Cole-Cole model parameters: Resistivity ρ, chargeability m, time constant τ and frequency dependence c which is a dimensionless quantity.

Number	ρ (Ωm)	m (mV/V)	τ(s)	c (-)
1	10	10	1	0.2
2	7	50	3	0.3
3	5	100	10	0.4
4	5	70	6	0.4
5	3	150	40	0.6

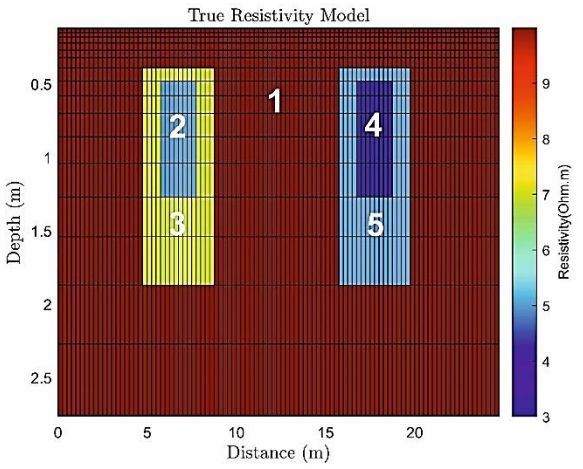

Figure 9. Representation of the third synthetic model used in [9] containing five different mediums.

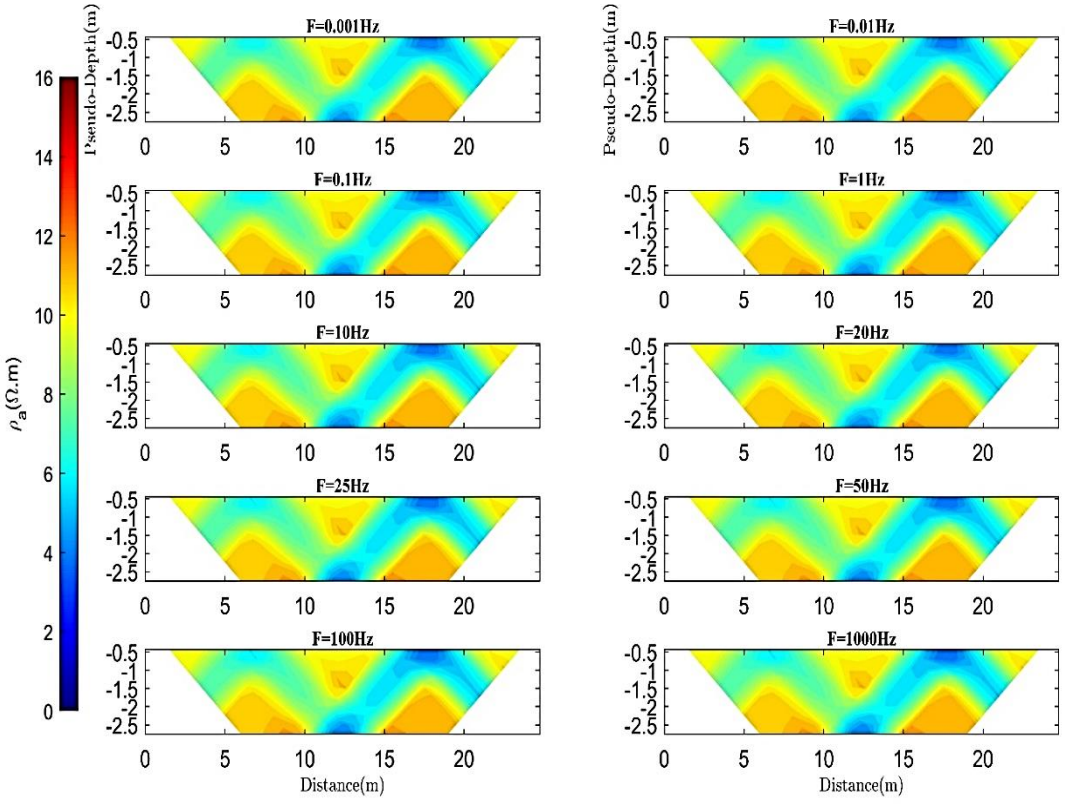

Figure 10. Apparent resistivity (amplitude) pseudo-sections for a broad frequency range related to the synthetic model shown in Fig.9, used in [9].

6. Conclusion

By using the SIP method and applying a defined broad range of frequencies, it is possible to describe items such as medium properties, spectral behavior, and the intensity of every single parameter. The broad application of the SIP method requires accurate and fast modeling and inversion algorithms. An accurate and efficient forward calculation is the basis of most inversion processes and it is a helpful means to enhance physical understanding of the subsurface structures. Like any other geophysical method, a reliable spectral induced polarization inversion and modeling is highly dependent on the accuracy of the forward problem. Hence, a general algorithm in the MATLAB programming language was developed to simulate the response of an arbitrary 2D distribution of the Cole-Cole model parameters for desired arrays of current and potential electrodes.

The proposed numerical method is based on the solution of Poisson's equation in the framework of the finite difference scheme. Our results proved that the forward responses, including the amplitude and phase values derived from the subsurface structures with different Cole-Cole model parameters are highly dependent on the variation of frequency values. We also compared the resistivity and phase pseudo-sections derived from the proposed algorithm with those obtained from the Geotomo geo-electrical forward modeling.

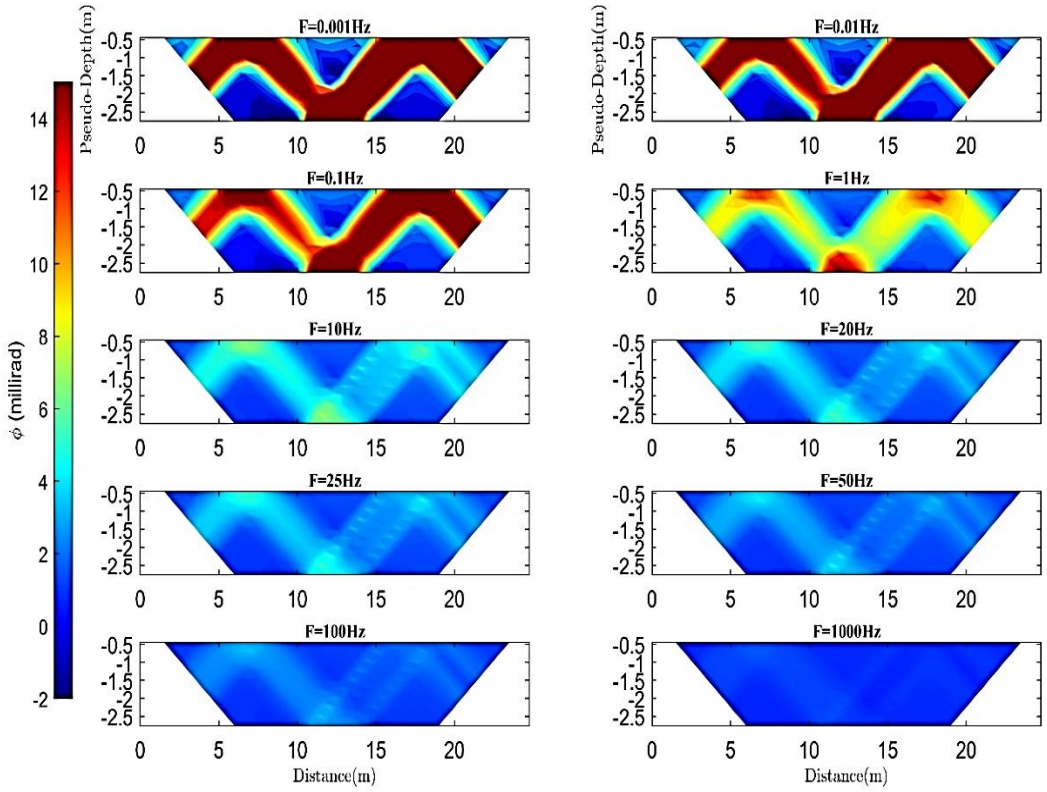

Figure 11. Phase angle pseudo-sections for a broad frequency range related to the synthetic model shown in Figure 9, used in [9].

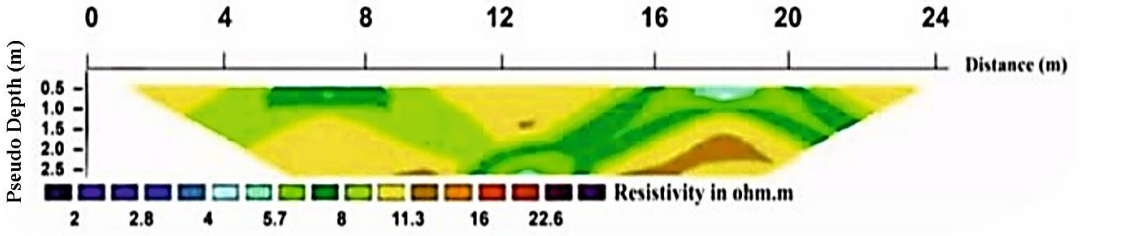

Figure 11. Apparent resistivity (amplitude) pseudo-section for the frequency of 1Hz derived by [9].

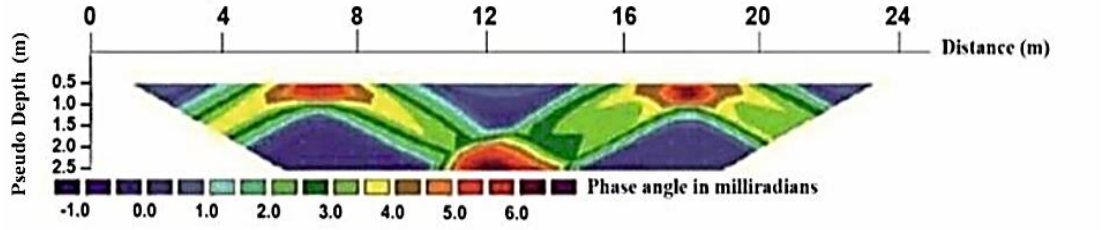

Figure 13. Phase angle pseudo-section for the frequency of 1Hz derived by [9].

REFERENCES

[1] Pelton, W. H, Rijo, L, Swift, J. R, 1978, Inversion of two-dimensional resistivity and induced polarization data. Geophysics, 681-904.

[2] Olsson, P.-I., Dahlin, T., Fiandaca, G., Auken, E., 2015. Measuring time-domain spectral induced polarization in the on-time: decreasing acquisition time and increasing signalto- noise ratio. J. Appl. Geophys. 123, 316–321.

[3] Revil, A., Karaoulis, M., Johnson, T., and Kemna., A., 2012, Review: Some low-frequency electrical methods for subsurface characterization and monitoring in hydrogeology: Hydrogeology Journal, 20(4), 617–658.

[4] Dey, A., Morrison, H.F., 1979, Resistivity modeling for arbitrary shaped two-dimensional structures, Geophysical Prospecting 27, 1020–1036.

[5] Zhang, J., Mackie, R. L., and Madden, T. R., 1995, 3-D resistivity forward modeling and inversion using conjugate gradients. Geophysics, 60(5), 1313-1325

[6] Lowery, T, Allen, M, B, Shive, P, N, 1989. Singularity removal: a refinement of resistivity modelling techniques. Gepphysics, 680-789.

[7] Weller A., Seichter M. and Kampke A. 1996. Induced-polarization modelling using complex electrical conductivities. *Geophysical Journal International* 127, 387-398

[8] Routh, P.S., Oldenburg, D.W., Li, Y., 1998. Regularized inversion of spectral IP parameters from complex resistivity data. In: 68th SEG Meeting, New Orleans, USA, Expanded Abstracts, pp. 810–813.

[9] Loke, M.H., Chambers, J.E., 2006, Inversion of 2D spectral induced polarization imaging data, Geophysical Prospecting, 54, 287–301.

[10] Kemna, A., Binley, A., Ramirez, A. L., Daily, W. D., 2000, Complex resistivity tomography for environmental applications.

[11] Rucker, C, Gunther, T, Spitzer, K, 2006, Three dimensional inversion of DC resistivity data incorporating topography. Geophysics Journal 2006.

[12] Xu, K. J., 2007, Study on 2.5D complex resistivity electromagnetic forward and in version: PhD Thesis, Jilin University.

[13] Farias, V. J., Maranhao, C. H., Andrade, P, O, Induced polarization forward modelling using finite element method and the fractal model, Elsevier. 2007.

[14] Rucker, C, Gunther, T, Spitzer, K, 2011, Three dimensional modelling of DC resistivity data incorporating topography. Geophysics Journal 2011.

[15] Zhang, Z. Y., Tan, H. D., Wang, K. P., Lin, C. H., Zhang,B. and Xie, M. B., 2016, Two-dimensional inversion of spectral induced polarization data using MPI parallel.

[16] Günther, T., Martin, Tina, 2016, Spectral two-dimensional inversion of frequency-domain induced polarization data, Journal of Applied Geophysics 135, 436–448.

[17] Fiandaca, G., Ramm, J., 2013, Resolving spectral information from time domain induced polarization data through 2-D inversion, Geophys. J. Int 192, 631–646.

[18] Kemna, Andres., 2004, Tomographic inversion of complex resistivity, theory and application.

[19] Ghanati, R., Azadi, Y., Fakhimi, R., 2020. RESIP2DMODE: A MATLAB-Based 2D Resistivity and Induced Polarization Forward Modeling Software, Iranian Journal of Geophysics 13 (4), 60-78.